*Pure Appl. Chem.*, Vol. 82, No. 11, pp. 2075–2095, 2010.
doi:10.1351/PAC-CON-09-11-08


# Pulsed electrodeposition and unique properties of one-dimensional Bi-based nanostructures in porous alumina membranes*

Liang Li‡, Xincun Dou, Hongqiang Wang, Guanghai Li‡, and Lide Zhang

*Key Laboratory of Material Physics, Anhui Key Laboratory of Nanomaterials and Nanotechnology, Institute of Solid State Physics, Chinese Academy of Sciences, P.O. Box 1129, Hefei 230031, China*

*Abstract*: One-dimensional (1D) Bi-based nanostructures are promising thermoelectric materials and, furthermore, are very interesting systems for studying physical and chemical properties in the nanoscale, owing to their anisotropic character. The main challenges in this area are to control the diameter, orientation, and alloy composition with precision, and thereby to gain ready access to junction and superlattice structures. Here, we review our recent contributions toward advances in pulsed electrodeposition-based routes to fabricate Bi-based nanostructures. As a main theme, porous anodic alumina membranes (AAMs) have been employed as effective templates to fabricate Bi elementary, alloy, junction, and superlattice structures, and unique properties are demonstrated.

*Keywords*: bismuth; nanotubes; nanowires; pulsed electrodeposition; superlattice.

## INTRODUCTION

Thermoelectric devices can convert electrical energy directly into a temperature gradient. This phenomenon was discovered by Peltier in 1834. Various practical thermoelectric refrigeration applications of this cooling or heating remained minimal until the development of semiconductor materials. The thermoelectric devices can also convert thermal energy directly from a temperature gradient into electric energy. This phenomenon was discovered in 1821 and is called the "Seebeck effect". When a temperature differential is established between the hot and cold ends of semiconductor material, a voltage is generated. This voltage is called the Seebeck voltage, and is directly proportional to the temperature differential. The constant of proportionality is referred to as the Seebeck coeffcient. Based on this Seebeck effect, thermoelectric devices can also act as power generators.

Thermoelectric devices have no moving parts and therefore need substantially less maintenance, sustain long steady-state operation, contain no chlorofluorocarbons or other materials that may require periodic replenishment, and can function in severe and sensitive environments. The foregoing properties ensure that thermoelectric devices have found very extensive applications, such as military, aerospace, instrument and industrial or commercial products.

*Paper based on a presentation at the 5th International Symposium on Novel Materials and Their Synthesis (NMS-V) and the 19th International Symposium on Fine Chemistry and Functional Polymers (FCFP-XIX), 18–22 October 2009, Shanghai, China. Other presentations are published in this issue, pp. 1975–2229.
‡Corresponding authors: E-mail: liliang@issp.ac.cn (L.L.); ghli@issp.ac.cn (G.L.)

The maximum efficiency of a thermoelectric material is determined by its dimensionless figure of merit ($ZT$): $ZT = S^2\sigma T/\kappa$, where $S$, $\sigma$, $T$, and $\kappa$ are, respectively, the Seebeck coefficient, electrical conductivity, temperature, and thermal conductivity. The quantities $S$, $\sigma$, and $\kappa$ for conventional three-dimensional (3D) crystalline systems are interrelated, so it is very difficult to control these variables independently to increase $ZT$, which is due to the fact that conventional 3D crystalline systems follow the Wiedemann–Franz law that an increase in $S$ usually results in a decrease in $\sigma$ and produces a decrease in the electronic contribution to $\kappa$. In the 1990s, theoretical predictions suggested that the thermoelectric efficiency could be greatly enhanced in one-dimensional (1D) and two-dimensional (2D) systems compared to the bulk materials, owing to both a sharper density of states in low-dimensional systems for enhanced thermopower ($S^2\sigma$) and an increased phonon scattering for reduced lattice thermal conductivity ($\kappa$). Recent experiments further showed that heterostructures and superlattices may result in higher $ZT$, because heterogeneous interfaces can reduce lattice thermal conductivity by increasing phonon scattering at segment interfaces. The thermopower can be enhanced owing to sharper density of states than 1D homogeneous nanowires.

Bismuth (Bi), with a rhombohedral crystal lattice structure, is a semimetal with a small effective electron mass, long carrier mean free path, highly anisotropic Fermi surface, and small energy overlap (about 38 meV at 77 K) between the L-point conduction band and the T-point valence band, which can lead to semimetal–semiconductor transition in Bi nanowires with decreasing diameter to a certain value (about 60 nm at 77 K) [1]. Both theoretical and experimental results showed that low-dimensional Bi could have an even larger enhancement in thermoelectric efficiency relative to the bulk one [2,3]. The combination of Bi element with antimony (Sb) and tellurium (Te) to form alloy, junction, and superlattice nanowires only starts to emerge recently, which was expected to demonstrate more excellent thermoelectric performances.

In the literature, there are a large number of reviews on the progress of thermoelectric materials, which will not be included here due to space limitation [4]. This article mainly focuses on our recent contributions to rational growth, characterization, and physical properties of 1D Bi-based nanowires, nanotubes, junctions, and superlattices. The main text of this article is organized into three sections. In the next section (Results and Discussion), we mainly discuss the fabrication, electrical transport, and thermal expansion properties of Bi nanostructures deposited by pulsed electrodeposition. Systematic control over the composition, diameter, and orientation of Bi nanostructures are discussed in detail. In the final section, we conclude this short review with personal perspectives on future research directions and focuses in 1D Bi nanostructures.

## RESULTS AND DISCUSSION

In this section, we mainly present some recent progresses in the fabrication and characterization of 1D Bi nanostructures using pulsed electrodeposition technique in the templates of anodic alumina membranes (AAMs), together with analyses of novel physical properties. Firstly, we try to introduce simply the fabrication procedure of AAMs.

The template-assisted synthesis is a conceptually simple and intuitive way to fabricate nanowires [5–12], besides the chemical vapor deposition, hydrothermal, et al. [13–17]. These templates contain very small cylindrical pores or voids within host materials, and the empty spaces are filled with chosen materials, which adopt the pore morphology, to form nanostructures. Among these templates, the AAM-based synthesis approaches have received considerable attention due to their several unique structure properties, such as controllable pore diameter, extremely narrow pore size distribution, and ideally cylindrical pore shape. Briefly, firstly a high purity aluminum sheet (99.999 %) was anodized at 40 V in 0.3 M oxalic acid electrolyte at 12 °C for 4 h. The alumina layer produced was removed by immersing it in a mixture of phosphoric acid (6 wt %) and chromic acid (1.8 wt %) at 60 °C for 6 h. The second anodization process was performed under the same conditions as the first one for 12 h. After the

 

anodization, the bottom aluminum substrate was removed in a saturated $SnCl_4$ solution, and then the alumina barrier layer was dissolved in 6 wt % phosphoric acid solution at 30 °C to get the final AAM with a pore size of about 40 nm. AAMs with the pore size larger than 40 nm can be obtained by a pore-widening treatment process in 5 wt % $H_3PO_4$ solution at 30 °C.

## Bi and Sb elementary nanowires and nanotubes

### *Bi nanowires*

A number of growth methods for Bi nanowires have been studied in an effort to understand their unique transport properties. Several template-based synthesis methods have been developed for the growth of Bi nanowires, including electrochemical deposition and pressure injection in nanochannels of AAM [18–20]. Due to the high anisotropy in Bi, it is important and interesting to obtain Bi nanostructures with different diameters and orientations, and then study their unique physical properties. Generally, to fabricate nanowires with different diameters, AAMs with different pore sizes are needed, nevertheless, AAMs with pore sizes less than 20 nm are very hard to fabricate and easily break into pieces. Our group has developed pulsed electrodeposition technique to fabricate Bi nanowires with diameters from 20 to 80 nm in the AAM with a pore size of 80 nm through modulating pulsed parameters [21,22].

Figure 1 shows typical transmittance electron microscopy (TEM) images of Bi nanowires fabricated by modulating the pulse turn-on time ($t_{on}$) from 5 to 30 ms and keeping the pulse turn-off time ($t_{off}$) at 50 ms. One can see that the corresponding diameter of Bi nanowires changes from about 6.5 to 40 nm, which are much smaller than the pore size (80 nm) of AAMs. Figures 1a–c show the presence of freestanding Bi nanowires embedded in pores of AAM. When $t_{on}$ was increased to 50 ms, the diameter of Bi nanowires increased to 80 nm, equaling the nanochannel size of AAMs (Fig. 1f). Corresponding selected-area electron diffraction (SAED) patterns inserted in these figures indicate that nanowires with diameters larger than 10 nm are single crystals, however, the nanowires with diameters less than 10 nm seem to be polycrystalline.

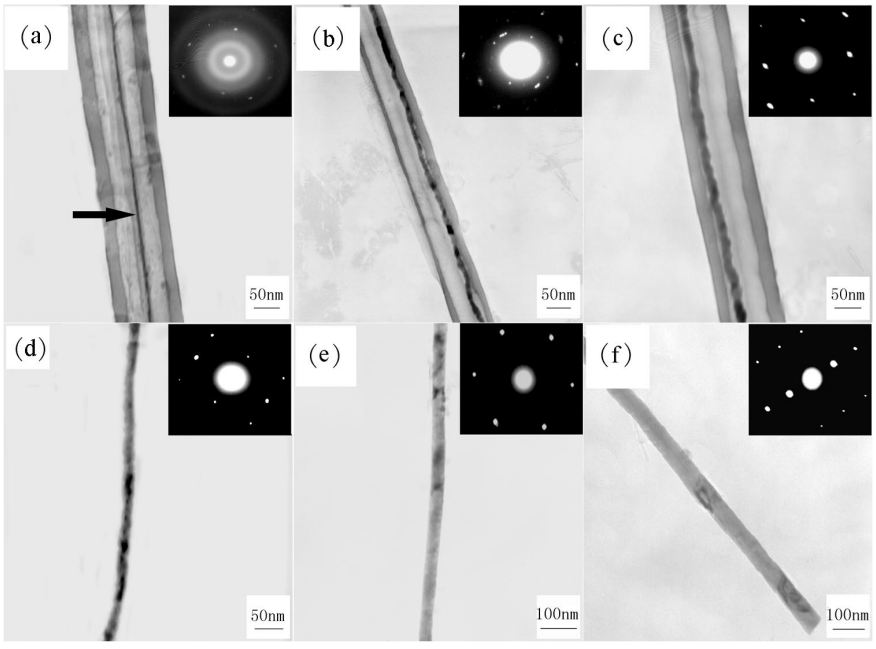


**Fig. 1** TEM images of Bi nanowires with different pulse parameters: (a) 5 ms, (b) 10 ms, (c) 20 ms, (d) 25 ms, (e) 30 ms, and (f) 50 ms.

 

The above results demonstrate that diameters of Bi nanowires can be controlled within a wide range through modulating the $t_{on}$ and keeping the $t_{off}$ fixed. Under a short $t_{on}$, the Bi ions provided for deposition are not enough to instantly cover all the area of each pore of AAM, resulting in part growth on the bottom of pores at the same time, Bi ions have not adequate time to transfer along the bottom area if $t_{off}$ is not long enough, thus, Bi nanowires with the smaller diameters are formed. Contrarily, if $t_{on}$ is long enough to provide adequate Bi ions, Bi nanowires with the corresponding pore size of AAMs are fabricated.

Because Bi nanowires with the diameters smaller than pore sizes of AAMs can be fabricated, namely, nanowires are free-standing in the nanochannels and not be affected by the restriction of pore walls of AAMs during measuring physical properties. To demonstrate advantages of this structure, thermal expansion properties of the above samples are shown [23]. Thermal expansion behavior of Bi nanowire arrays with different diameters was performed by in situ high-temperature X-ray diffraction (XRD) (Philips PW 1700×) in the temperature range from 300 to 500 K under high vacuum atmosphere. From the XRD pattern and Bragg equation, $2d\sin\theta = \lambda$ ($d$, $\theta$, and $\lambda$ are the interplanar spacing, diffraction angle, and X-ray incidence wavelength, respectively), the lattice parameters $d$ can be calculated, which are shown in Fig. 2. One can see that the lattice parameter firstly increases with increasing temperature and then decreases at a certain temperature for Bi nanowires with diameters in the range 20–60 nm, and there is a critical transition temperature, $T_c$, at which the temperature coefficient of lattice parameter changes from positive to negative (see Figs. 2a–c). The $T_c$ shifts to high temperature with increase in diameters from 20 to 60 nm. The lattice parameter of Bi nanowires with a diameter of 10 nm always decreases with increasing temperature and there is not a transition temperature, while that with a diameter of 80 and 250 nm always increases. These results indicate that Bi nanowires with a very small diameter might possess a negative thermal expansion behavior even at room temperature region. After fitting the experimental data with the fourth-order polynomial, $a = \sum_{n=0}^{4} a_n T^n$, as shown in Fig. 2c (dashed lines), the obtained coefficients $a_n$ can be used to calculate the thermal expansion coefficient. The thermal expansion coefficient is defined by

$$\alpha = \frac{1}{a_0}\frac{\partial a}{\partial T} = \frac{1}{a_0}\left(a_1 + 2a_2T + 3a_3T^2 + 4a_4T^3\right) \tag{1}$$

The $\alpha(T)$ curves of Bi nanowires with different diameters are also plotted in Fig. 2d. It can be clearly seen that the Bi nanowires have either positive or negative thermal expansion coefficient depending on temperatures and diameters of Bi nanowires, and the transition temperature of thermal expansion coefficients from positive to negative is consistent with that obtained from the lattice parameter.

The positive thermal expansion is commonly observed in most bulk material, which can be understood by accounting for effects of the anharmonic lattice potential on the equilibrium lattice separations and characterized by the Gruneisen parameter. Our results prove that the lattice thermal contraction is an intrinsic property of Bi nanowires.

 

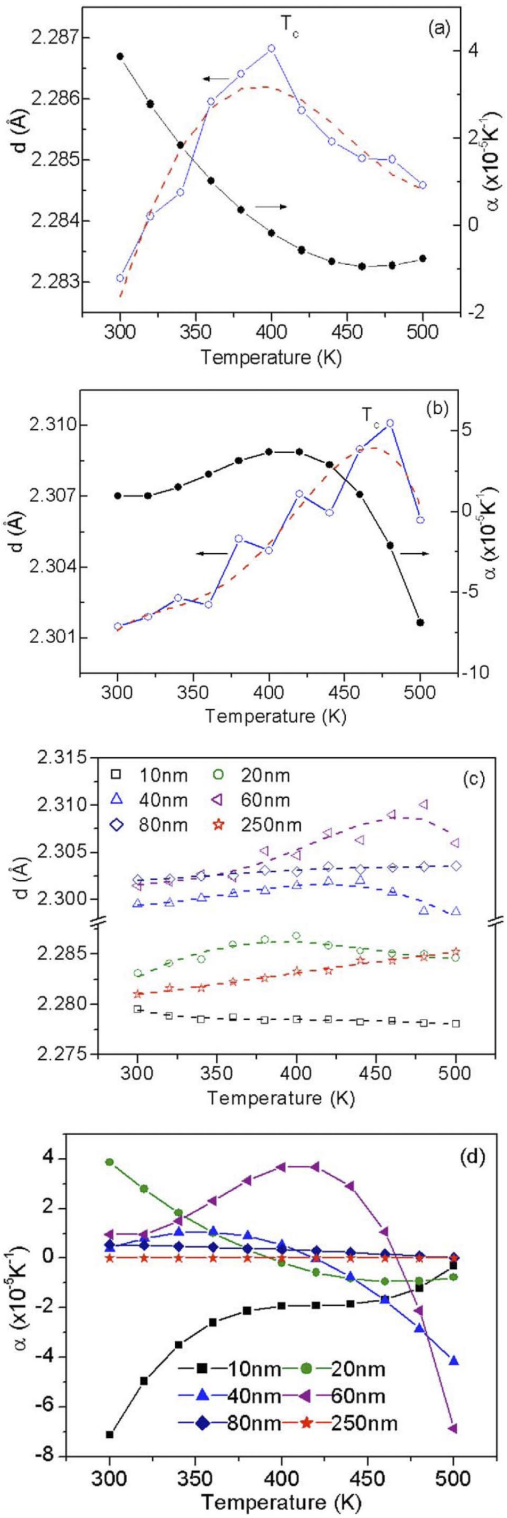


**Fig. 2** Temperature dependences of lattice parameter $d$ and thermal expansion coefficient $\alpha$ of Bi nanowires with different diameters.

*Bi nanotubes*

Nanotubes have a strong phonon blocking effect due to their structure features of both hollow tube channels and 2D tube walls, resulting in the reduced lattice thermal conductivity and different electronic transport behaviors from nanowires, and an improved thermoelectric efficiency thus could be expected. Recently, Bi nanotubes have been synthesized by low-temperature hydrothermal and solvothermal approaches [24,25]. The schematic illustration of our fabrication processes of Bi nanotubes is shown in Fig. 3a [26]. To grow Bi nanotubes, thin Au film needs to be sputtered mainly on the top part of the inner pore surface and covers only a few parts of the pore of AAM, which can be controlled by the deposition rate and time, as shown in Fig. 3b. The subsequent growth of Bi preferentially takes place only on these Au covered areas, resulting in the growth of Bi along the pore wall of the AAM, and thus forms a tubular nanostructure.

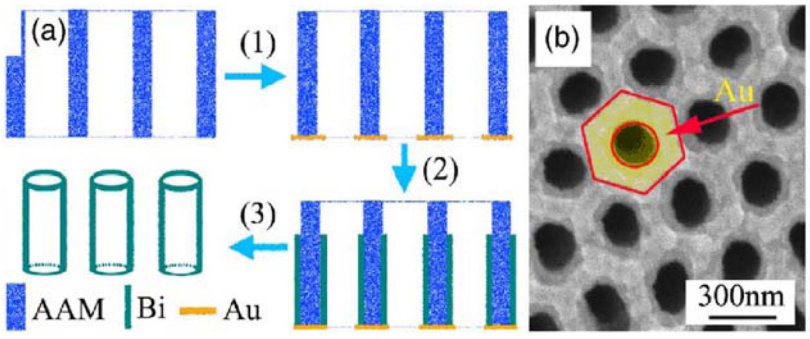


**Fig. 3** (a) Schematic illustration of the growth processes of Bi nanotube arrays: (1) sputtering thin Au electrode film, (2) electrodepositing Bi nanotube, and (3) removing AAM, and (b) typical SEM image of AAM with thin Au electrode film sputtered.

The temperature dependence of the resistance $R(T)$ of Bi nanotubes arrays with the same wall thickness (15 nm) but with the different diameters of 40, 90, and 250 nm, normalized to the resistance at 300 K, is shown in Fig. 4a. One can see that the resistances of all the Bi nanotubes decrease with increasing temperature and exhibit an obvious negative temperature coefficient of resistance (*TCR*), i.e., a typical semiconductor-like character, which suggests that all the Bi nanotubes have a semiconductor character. To further elucidate this problem, we measured the resistances of Bi nanotubes with the same diameter (250 nm) but with the different wall thickness (15, 75, and 100 nm), as shown in Fig. 4b. It is noticed that the 15-nm Bi nanotubes have a negative *TCR*, while the 100-nm nanotubes have a positive *TCR*. The 75-nm nanotubes have a transition from a positive *TCR* at low temperatures ($T < 225$ K) to a negative one at high temperatures ($T > 225$ K).

The electronic transport properties of Bi nanotubes depend only on the wall thickness and are independent of the diameters of nanotubes, and the semimetal–semiconductor transition occurs as the wall thickness decreases from 100 to 15 nm. For the Bi nanotubes with the wall thickness of 100 nm, the *TCR* is positive and is quite similar to bulk Bi, because the carriers undergo a weak quantum confinement effect in the relatively thick tube walls, the phonon-limited mobility decreases with temperature almost as a $T^4$ law, even though the electron and hole densities increase by about one order of magnitude [27]. The Bi nanotubes with the wall thickness of 75 nm show a semimetal behavior and have a positive *TCR* below 225 K, where the carrier density is rather temperature-independent and phonon scattering contributes to a negative temperature coefficient of mobility. The dominant scattering mechanism for carriers is nanotubes boundary scattering, and thus the carrier free path and mobility is relatively insensitive to $T$. At temperatures above 225 K, the carrier density largely increases with $T$, and since the boundary scattering dominates, the temperature dependence of the carrier mobility in nano-

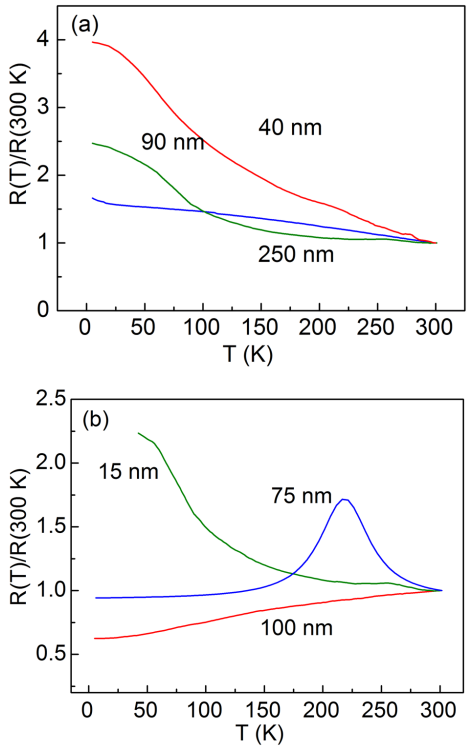


**Fig. 4** Temperature dependence of the normalized electronic resistances of Bi nanotube arrays (a) with the same wall thickness 15 nm and different diameters and (b) with the same diameter of 250 nm and different wall thickness.

tubes is much weaker than that in bulk Bi, and a negative *TCR* was observed. The Bi nanotubes with the wall thickness of 15 nm have a negative *TCR* over the entire temperature range and have a semiconductor character, implying that the carrier is temperature-dependent at all the temperatures. Based on the above experimental and analytic results, the Bi nanotubes should undergo a metal–semiconductor (M–S) transition as the wall thickness of nanotubes decreases to a certain value due to the strong quantum confinement effect.

### *Sb nanowires*

Systematical study indicates that the pulsed electrodeposition with optimal electric parameters and growth conditions (as shown in Table 1) can fabricate Sb nanowire arrays with different diameters and high filling rate in AAM [28,29].

**Table 1** Growth conditions for single-crystalline Sb nanowire arrays with different diameters.

| Current density ($mA/cm^2$) | Nanowire diameter (nm) | Density ($cm^{-2}$) | Growth time (h) |
|---|---|---|---|
| 12 | 40 | $2.9 \times 10^{10}$ | 18 |
| 10 | 30 | $4.7 \times 10^{10}$ | 7 |
| 4.7 | 15 | $2.6 \times 10^{11}$ | 0.5 |
| 4.2 | 9 | $2.9 \times 10^{11}$ | 0.3 |

 

Figure 5 shows a typical TEM image of single-crystalline Sb nanowires with 30 nm diameter. Figure 6 shows a high-resolution TEM (HR-TEM) image of 40 nm diameter Sb nanowire. Extremely high structural quality of the Sb nanowire can be seen from the clear image of 2D lattice planes. Figure 7 shows the temperature dependence of the resistance $R(T)$ of single-crystalline Sb nanowire arrays with different diameters, normalized to the resistance at 273 K. One can see that the resistances for 40 and 30 nm Sb nanowires increase with temperature, and exhibit a positive *TCR*, i.e., typically a metal-like

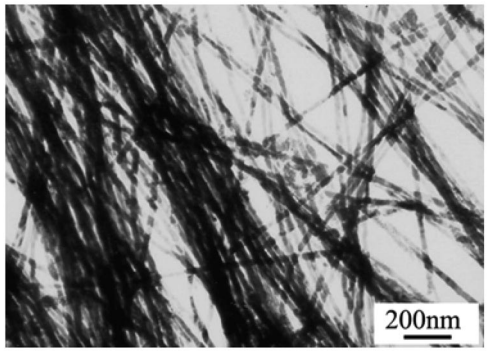


**Fig. 5** Typical TEM image of 30-nm single-crystalline Sb nanowires.

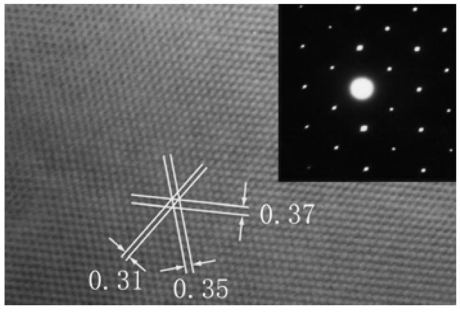


**Fig. 6** HR-TEM image and SAED pattern of a single 40-nm Sb nanowire.

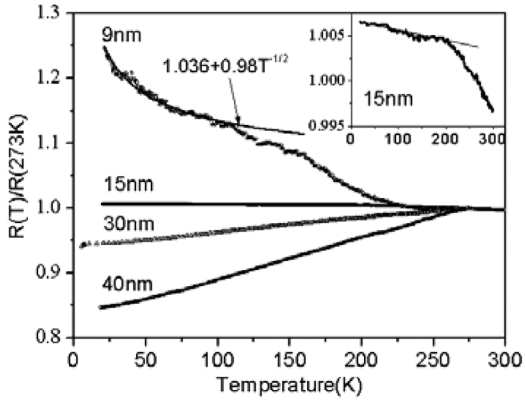


**Fig. 7** Temperature dependence of the resistance of Sb nanowire arrays with different diameters. The inset is a plot for 15-nm Sb nanowires.

character, and the temperature dependences are weak. The $R$(T) for 15 nm (see also the inset in Fig. 7) and 9 nm Sb nanowires exhibit a negative *TCR* behavior, i.e. a semiconductor-like character, and the negative *TCR* is not exponential. The resistance for the 9-nm Sb nanowires follows essentially a $T^{-1/2}$ law at temperatures lower than 110 K (see the dashed line in Fig. 7). It is known that both the carrier mobility and the concentration contribute to the *TCR* value, and the two factors have opposite temperature dependence. For 40- and 30-nm nanowires, the carrier density is a weak function of temperature and the $R(T)$ is mainly controlled by the temperature dependence of the carrier mobility under the competition of various scattering mechanisms. The electron-boundary scattering, being relatively $T$-independent, dominates at lower temperatures, and the electron-phonon scattering becomes dominant at higher temperatures and increases with temperature. The decrease in the diameter of Sb nanowire will lead to a stronger infinite size effect, which enhances the weak localization behavior at lower temperature. Besides the weak localization, other mechanisms might also contribute to the temperature dependence of resistances. But we consider that the weak localization is the main mechanism in determining the temperature dependence of resistances of single-crystalline Sb nanowires.

## Bi, Sb, and Te alloy nanowires

### *$Bi_{1-x}Sb_x$ nanowires*

Theoretical calculations have indicated that Bi and its related alloys are promising candidates for low-dimensional thermoelectric materials at about 100 K, and desirable *ZT* values can be realized for $Bi_{1-x}Sb_x$ nanowires with diameters at about 35–50 nm, depending on the Sb mole fraction, $x$. $Bi_{1-x}Sb_x$ alloys are among the best $n$-type low-dimensional TE materials, and the maximum *ZT* is found for alloys with 12 % Sb ($ZT$ = 0.88) at 80 K. Here, the high-filling, large-area, and uniform $Bi_{1-x}Sb_x$ nanowire arrays were deposited into nanochannels of AAM from nontoxic aqueous solutions using the pulsed electrodeposition technique [30].

Figure 8 shows the typical XRD patterns of as-prepared $Bi_{1-x}Sb_x$ nanowire arrays. Figure 8a shows the XRD pattern of the $Bi_{0.89}Sb_{0.11}$ nanowire array deposited from the solution with Bi:Sb ratio of 5:2. All the peaks can be indexed to the rhombohedral space group Rm (to which Bi, Sb, and Bi–Sb alloys belong). These peaks are shifted to higher $2\theta$ values from the positions expected for a pure Bi sample, which is consistent with the formation of a solid solution. Figure 8b shows the XRD pattern of the $Bi_{0.15}Sb_{0.85}$ nanowire array deposited from the solution with Bi:Sb ratio of 2:5. Compared with pure Sb sample, all the peaks are shifted to lower $2\theta$ values as expected. The morphologies of the $Bi_{1-x}Sb_x$ nanowire arrays after etching for different times show that nanowires have a high filling-rate and the exposed parts of nanowires increase with the etching time, and all the $Bi_{1-x}Sb_x$ nanowires stand on the Au cathode at the bottom of pores with the same length, which implies that all the nanowires are deposited along the pores at the same rate (Fig. 9).

 

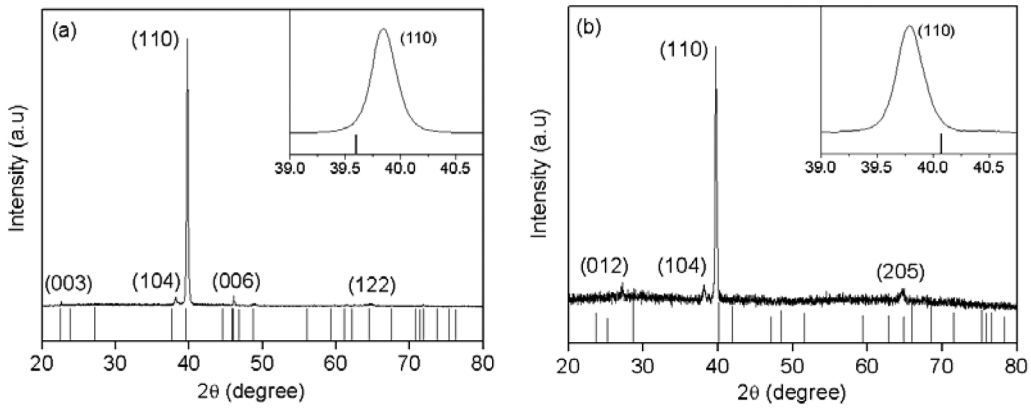


**Fig. 8** XRD patterns of Bi–Sb nanowire arrays. The insets show the shift of the (110) peak relative to the standard peak positions.

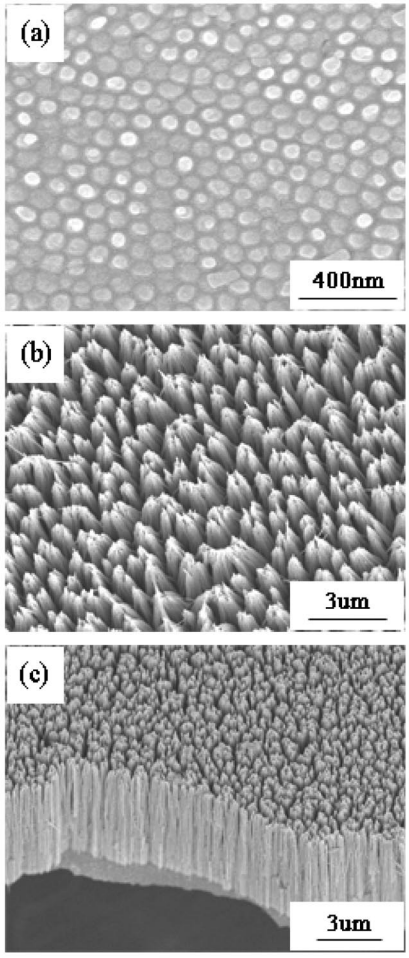


**Fig. 9** SEM surface and cross-section images of Bi–Sb nanowire arrays after different etching time of (a) 2 min, (b) 5 min, and (c) 10 min.

### *$Bi_2Te_3$ nanowires*

Bismuth telluride ($Bi_2Te_3$) and its solid solutions are well-known good TE materials for near-room-temperature applications. Bulk $Bi_2Te_3$ has a good TE figure-of-merit and has been widely used in commercial applications. Theoretical studies suggest that 1D $Bi_2Te_3$ nanowires may have a higher figure-of-merit than that of bulk materials, which have stimulated study in the fabrication of $Bi_2Te_3$ nanowire arrays [31–34].

Figure 10 shows the SEM images of $Bi_2Te_3$ nanowire arrays after etching in 0.5 M NaOH solution for different times. The bottom surface image of nanowire arrays after mechanically polishing with $Al_2O_3$ nanopowders and then etching for 2 min indicates that the nanowires are high filling (nearly 100 %, Fig. 10a). The surface image of nanowire arrays after etching for 8 min shows that all the nanowires have the same height, implying that the pulsed electrodeposition process is well controlled and all the nanowires grow along the pores at the same rate (Fig. 10b). The cross-sectional view of

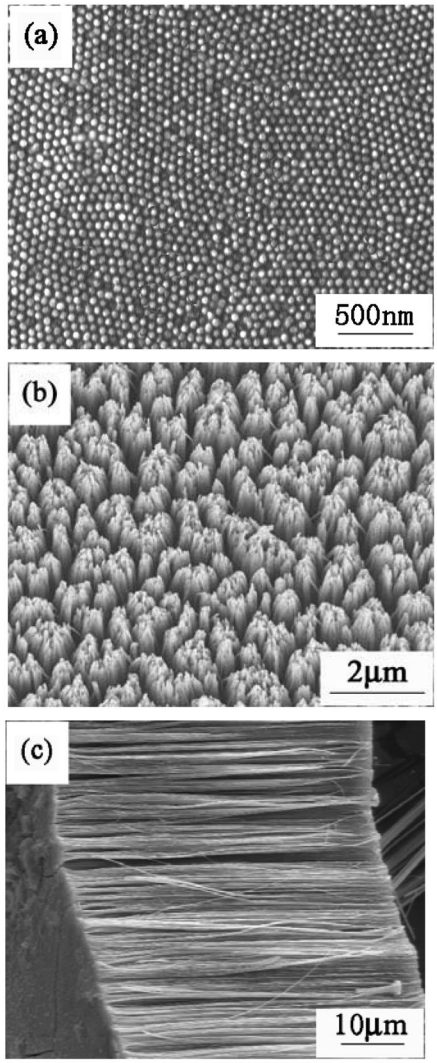


**Fig. 10** SEM images of $Bi_2Te_3$ nanowire array: (a) bottom view, (b) surface view, and (c) cross-sectional view.

nanowire arrays after etching for 15 min shows that the length of nanowires is about 50 μm (Fig. 10c), corresponding to the thickness of AAMs.

Figure 11 shows the variation of electrical resistance as a function of temperature for $Bi_2Te_3$ nanowires with the diameter of 40 nm (Fig. 11a) and 60 nm (Fig. 11b). One can see that the electrical resistances decrease with temperature, and exhibit a negative *TCR*, i.e., a typical semiconductor-like character. From Fig. 7 one can obtain the *TCR*s of $Bi_2Te_3$ nanowires, which are about $-1.25 \times 10^{-4}$ and $-2.16 \times 10^{-3}$ /K for 40- and 60-nm nanowires, respectively. The *TCR* of 40-nm nanowires is much smaller than that of 60-nm nanowires, indicating that the nanowires with smaller diameter have lower resistance sensitivity to temperature. The near linear dependence of In*R* on 1/*T* shown in the insets in Fig. 11 further proves that $Bi_2Te_3$ nanowires with the diameters of 40 and 60 nm all exhibit the normal semiconducting behavior.

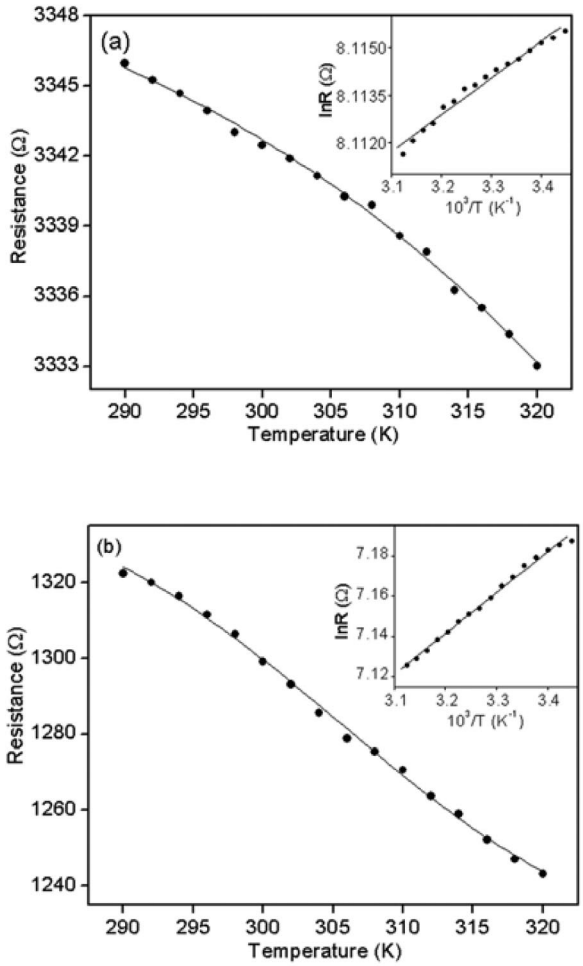


**Fig. 11** Temperature dependence of the electrical resistance for $Bi_2Te_3$ nanowires with different diameters: (a) 40 nm and (b) 60 nm.

## Bi–Bi, Sb–Bi, and BiSb alloy junctions and superlattices

### *Bi–Bi nanowire homojunction*

In the first step, Bi nanowires with the diameter corresponding to the pore size of AAMs were deposited, and then Bi nanowires with the diameter smaller than the nanochannel size of AAMs were subsequently fabricated through decreasing the $t_{on}$ in the first step [35].

The Bi–Bi segment nanowire homojunctions fabricated are shown in Fig. 12. Figure 12a shows the Bi junction nanowire with the diameters of 45 and 25 nm fabricated in AAMs with the pore size of 45 nm using, respectively, the $t_{on}$ of 35 and 26 ms and at constant $t_{off}$ of 40 ms, and Fig. 12b shows Bi junction nanowires with two segments of 100 and 35 nm in diameter fabricated in AAMs with the pore size of 100 nm using, respectively, the $t_{on}$ of 70 and 28 ms and constant $t_{off}$ of 50 ms. From the electronic transport properties of Bi nanowires, we know that the semimetal–semiconductor transition will occur when the diameter of Bi nanowires reduces to 60 nm, which suggests that the Bi junction nanowires shown in Fig. 12a has a semiconductor–semiconductor (S–S) junction character and that in Fig. 12b has an M–S junction character.

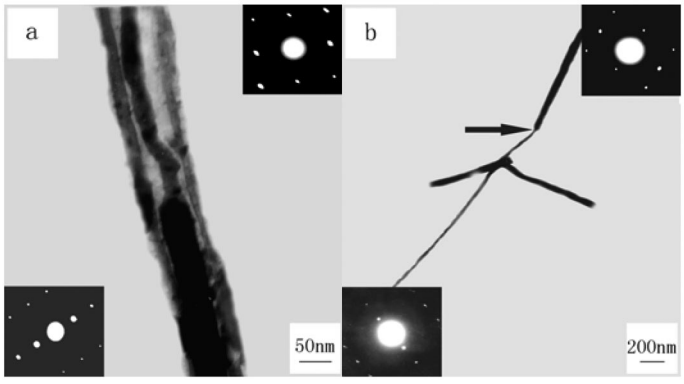


**Fig. 12** TEM images of Bi nanojunction nanowires: (a) S–S junction and (b) M–S junction.

Figure 13 shows the typical *I–V* plots for the Bi M–S junction nanowire array with two segments of 100 and 35 nm in diameter and Bi nanowire array with the diameter of 100 nm. The *I–V* curve of junction arrays shows an intrinsic nonlinear and asymmetric behavior at room temperature, but does not

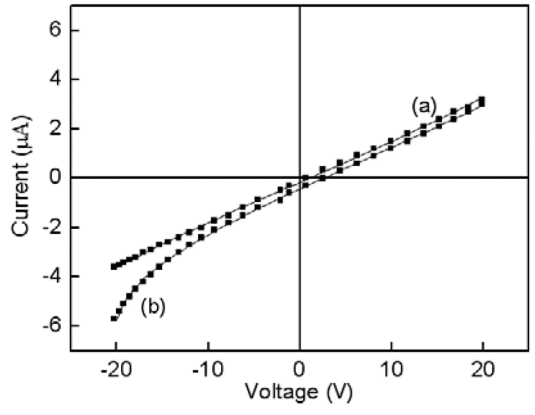


**Fig. 13** *I–V* curves of (a) Bi metal nanowire array and (b) Bi M–S junction nanowire array.

pass through the zero point (due to charging effect in the apparatus, curve b in Fig. 13). To assess the effect of contacts, we performed similar measurements on the arrays of straight Bi nanowire, and as expected that the *I–V* curve of the straight Bi nanowire arrays is linear and almost symmetric (curve a in Fig. 13), which provides further evidence that the observed nonlinear behavior is an inherent property of the Bi M–S junction nanowire arrays.

### *Sb–Bi nanowire heterojunction*

The Sb–Bi nanowire nanojunction arrays were prepared in AAMs by firstly depositing Sb followed by Bi using pulsed electrodeposition technique [28]. Figure 14 shows a typical TEM image of a single Bi–Sb segment nanowire junction. The clear nanocontact between the Bi and Sb nanowire can be seen. The corresponding SAEDs indicate the single-crystalline structure.

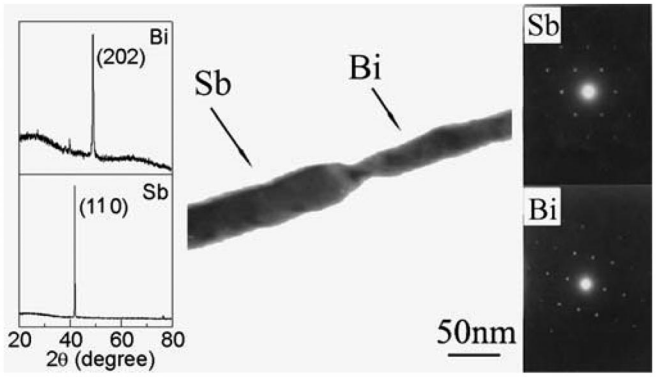


**Fig. 14** XRD patterns and TEM image of a single Bi–Sb segment nanowire nanojunction and corresponding SAED patterns of a Sb segment nanowire and a Bi segment nanowire.

Figure 15a shows the *I–V* curve of the Sb–Bi segment nanowire junction array at room temperature. A nonlinear transport characteristic can be observed at lower voltage as compared with a linear feature at higher voltage. A very thin transitional (or alloying) layer maybe was formed at the interface of two segment nanowires during the deposition. This nanocontact region has a different electric transport property; we speculate that the carrier density and band structure of the nanocontact region play an important role. The voltage remains small until the breakdown of the transitional layer at high current,

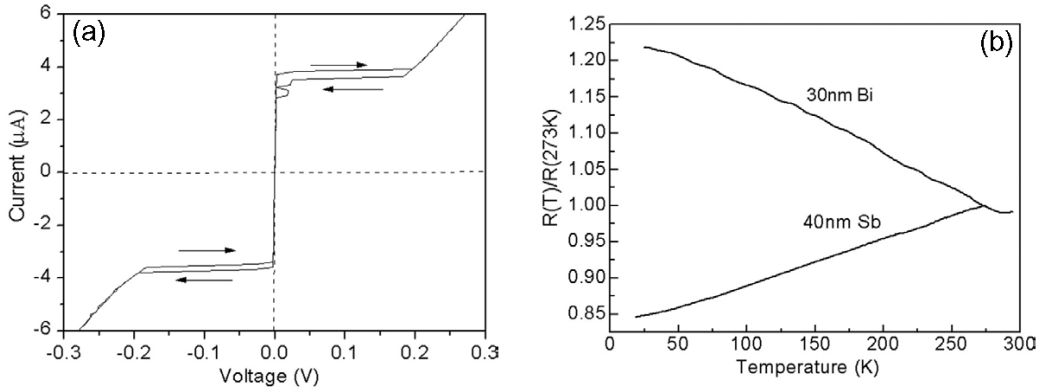


**Fig. 15** (a) *I–V* curve of Sb–Bi segment nanowire nanojunction array at room temperature. (b) Temperature dependence of resistance ratio $R(T)/R(273\ \mathrm{K})$ of Sb and Bi nanowire arrays at zero magnetic field.

which indicates that no M–S junction exists between Sb and Bi because there is no rectifying effect between the nanocontacts, and at higher voltage, i.e., the linear zone, the nanocontact exhibits an Oohmic effect.

### *BiSb nanotube–nanowire junction*

Figure 16 shows SEM images of the AAM with partially covered Au electrode–film and the BiSb alloy array in which the AAM pores still can be clearly seen [36]; see Fig. 16a (the back-side view) and Fig. 16b (the top-side view). The top-side view (Fig. 16c) clearly demonstrates that the top ends of alloy nanowire arrays, while the bottom-side view (Fig. 16d) displays the formation of nanotubes at the bottom of arrays. This result indicates that the as-prepared BiSb alloy array is a nanotube–nanowire junction array. Figure 17 shows the TEM image of a nanotube–nanowire junction. The junction contains a polycrystalline nanotube–nanowire segment with a length of about 820 nm (the nanotube is about 360 nm) and a single-crystalline nanowire segment with a diameter of about 70 nm; see Fig. 17a. The HR-TEM image of the nanotube section (Fig. 17b), corresponding to the first rectangle in Fig. 17a, shows some small grains on the wall, implying a polycrystalline structure. The HR-TEM image of the junction area of the polycrystalline nanotube–nanowire (Fig. 17c), the second rectangle in Fig. 17a, still shows some small grains, and the corresponding fast Fourier transform (FFT) (Fig. 17g) displays two diffraction points and does not change significantly in the whole area of the HR-TEM image. The HR-TEM image of the nanowire area (Fig. 17d, the third rectangle in Fig. 17a), clearly shows the transition of the nanowire from polycrystalline to single-crystalline structure. The HR-TEM image of the single-crystalline nanowire section (Fig. 17e), the fourth rectangle in Fig. 17a shows a clear lattice fringe, and the corresponding diffraction points (Fig. 17i) are sharp and bright, indicating the single-crystalline structure. To study the initial growth of the nanotubes, a very short deposition time was performed, and the obtained array only has an average length of about 300 nm. SEM top-side view

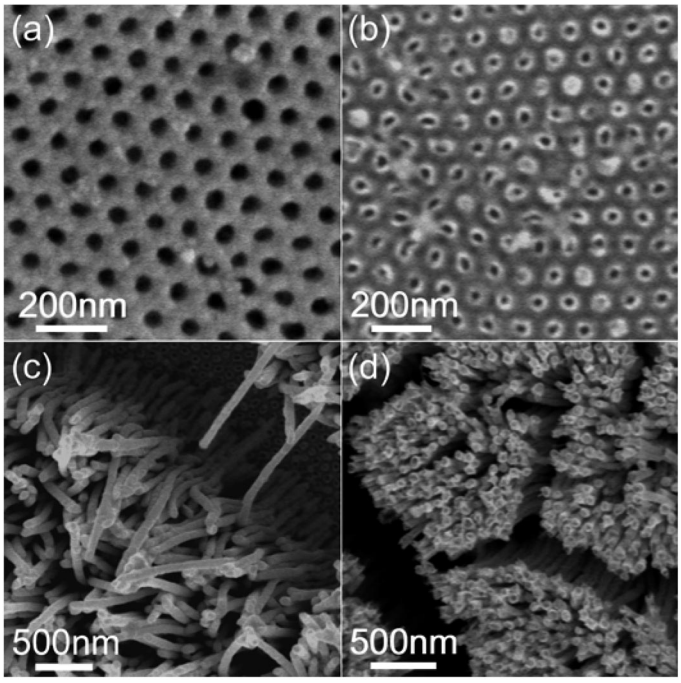


**Fig. 16** SEM images of (a) back-side of the AAM with partially covered Au electrode film, (b) top-side of the Au electrode after AAM totally dissolved, (c) top-side and (d) bottom-side views of the BiSb alloy nanotube–nanowire arrays after AAM completely dissolved.

 

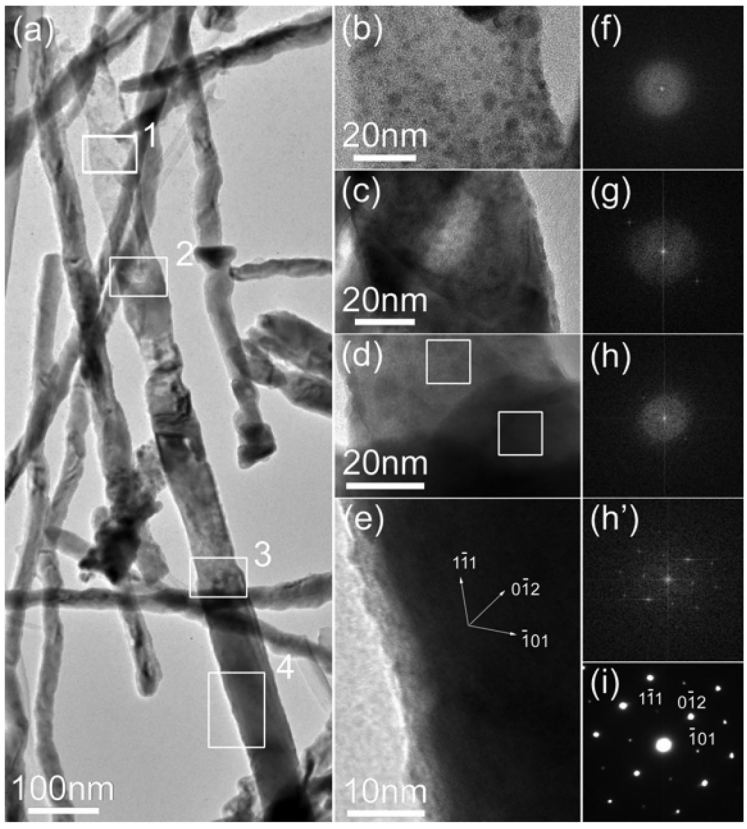


**Fig. 17** Typical TEM and HR-TEM, images of a single nanotube–nanowire junction, and corresponding FFT and SAED patterns.

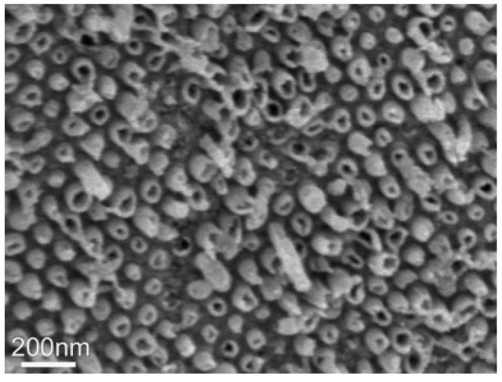


**Fig. 18** SEM image of a BiSb nanotube array with AAM dissolved totally.

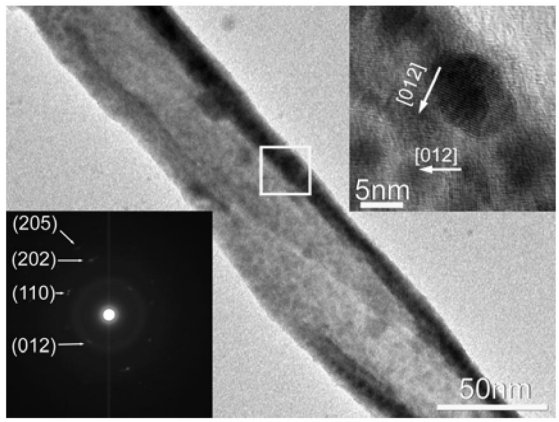


**Fig. 19** TEM image of a polycrystalline nanotube with the corresponding HR-TEM image and SAED pattern.

(Fig. 18) clearly demonstrates that the initial grown array is a nanotube. Figure 19 shows the TEM image of the nanotubes in which the corresponding SAED pattern (shown in the bottom inset) clearly shows a ring shape, proving that the nanotubes have a polycrystalline structure. The lattice fringes in different areas corresponding to different grains also can be clearly seen in the HR-TEM image (the top inset, two grains have different [012] orientations), which further proved the polycrystalline structure of the nanotubes.

### *Bi–BiSb superlattices*

We adopt the charge-controlled pulse electrodeposition to fabricate $Bi/Bi_{0.5}Sb_{0.5}$ superlattice nanowires in a two-electrode plating cell [37,38]. Briefly, the lower and higher pulse potentials are set by a computer-controlled pulse potential signal generator, the computer instantaneously integrates the current that the Real Time Current Acquisition System acquired to get the electric charge that passes during each time interval and subsequently monitors the pulse potential signal generator.

Figure 20 shows typical TEM images of epitaxial Bi–BiSb superlattice nanowires with a plane growth mode, in which the darker sections correspond to pure Bi segments and the brighter sections correspond to BiSb segments. The modulated structure of Bi–BiSb superlattice nanowires can be clearly seen in panels a and b of Fig. 20. The sharp and obvious interfaces were clearly manifested in Fig. 20c, in which the bilayer thickness is consistent along the whole nanowire. The corresponding SAED patterns shown in the upper insets of panels a and b of Fig. 20 indicate that the superlattice nanowires is single crystalline. Furthermore, HR-TEM observations show no dislocations along the interface, verifying a strictly epitaxial growth of the superlattice nanowires. According to the traditional 3D to 2D growth mode, the direction of the initial 2D growth plane, which is a result of nucleation and competition between different planes, should be parallel to the wire axis. In Fig. 20, the interfaces of Bi and BiSb layers are strictly normal to the nanowire axis, we believe this kind of growth mode is consistent with the traditional 2D plane growth mode of the electrodeposited nanowires. This growth process is a thermodynamic equilibrium state under the specific growth conditions and is controlled by thermodynamics. Otherwise, the 3D island morphology should be observed, and it is consistent with the layer-by-layer growth mechanism in molecular beam epitaxy.

 

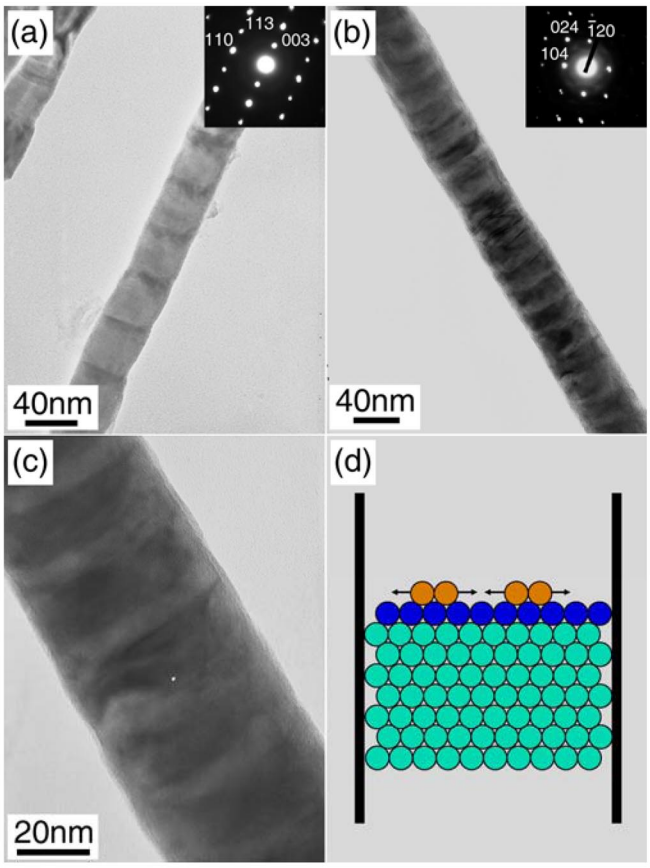


**Fig. 20** Typical TEM images of epitaxial Bi–BiSb superlattice nanowires with a plane growth mode. (a–b) TEM images of low magnification. (c) Higher magnification TEM image of (b). (d) Schematic representation of a 2D plane growth mode. The dark atoms represent the growth front and the growth plane of a superlattice nanowire, and the atoms above them represent the nucleus center of the 2D plane growth. The arrows represent the extending of nucleus in the plane.

The *I–V* curves of the superlattice nanowire arrays were recorded as a two-point measurement at room temperature, as schematically shown in Fig. 21a. Two typical samples were selected: One has a larger bilayer thickness (the average segment lengths of Bi and BiSb are, respectively, 15 and 20 nm, designated as SL1), and the other has a small bilayer thickness (the average segment lengths of Bi and BiSb are, respectively, 10 and 5 nm, SL2). The *I–V* curve is almost symmetrical with respect to the polarity of the applied current and follows a highly nonohmic relation (Fig. 21b), resembling a M–S diode. This nonlinear increase is caused by the Schottky barriers between the superlattice nanowires and the metal electrode in the semiconducting nanowire device. To further analyze the electrical transport properties of the superlattice nanowires, the applied current range was narrowed from −0.75 to +0.75 mA, and the results are shown in Figs. 21c,d, together with that after the annealing treatment. SL1 exhibits an obvious M–S Schottky characteristic in comparison with SL2, and the annealing treatment has almost no influence on the *I–V* response, indicating that the annealing treatment does not cause a phase separation of the BiSb segment nanowires and an obvious change in the electrical contacts between the metal and the Superlattice nanowires.

Figure 22 shows the typical *I–V* curves of individual superlattice nanowires in samples SL1 and SL2. The slope of the *I–V* curve for sample SL1 remains nearly zero at an applied voltage lower than

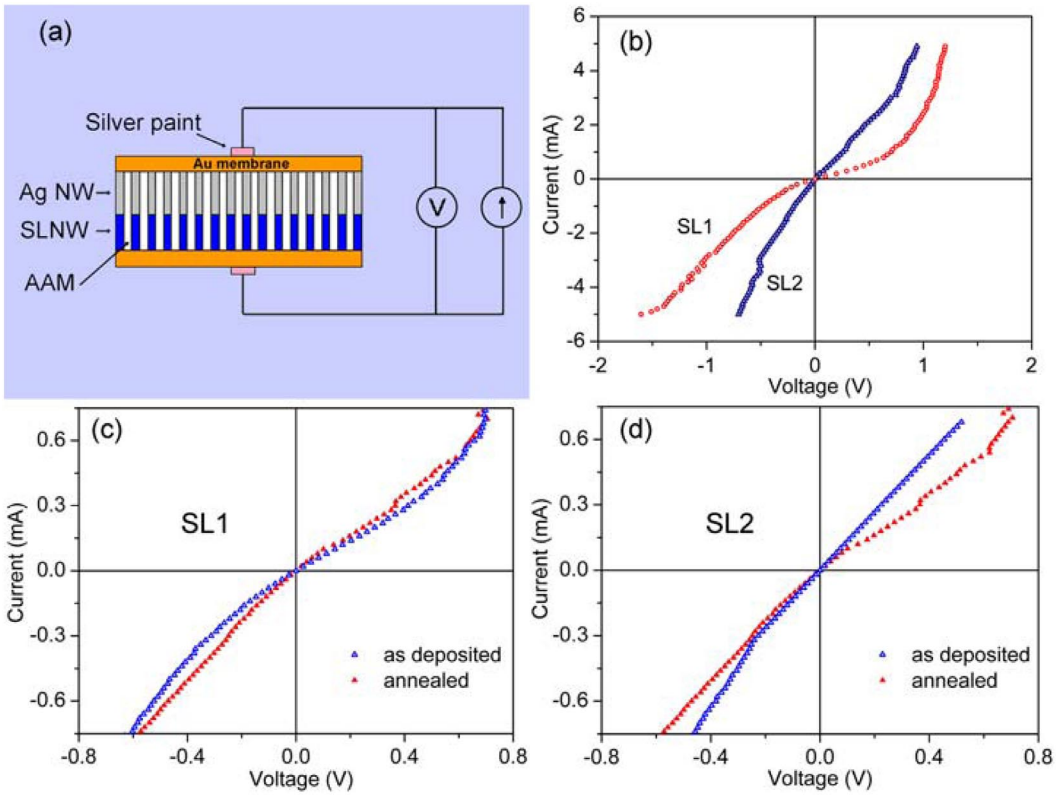


**Fig. 21** (a) Schematical illustration for the *I–V* curve measurement of the SLNW arrays. (b) *I–V* curves of sample SL1 and SL2. (c) and (d) *I–V* curves of as deposited and annealed sample SL1 and SL2.

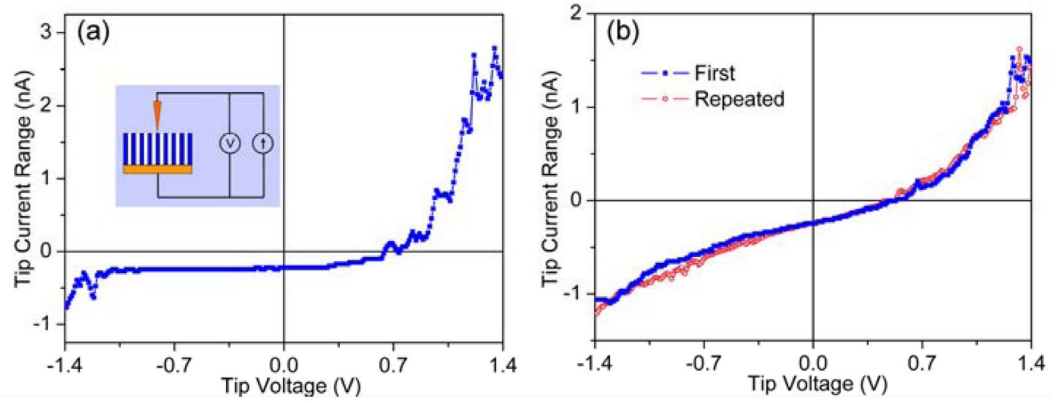


**Fig. 22** *I–V* response of individual SLNW embeded in the AAM by STM probe for sample (a) SL1 and (b) SL2.

0.35 *V* and increases dramatically at the applied voltage higher than 0.35 *V*, while that for sample SL2 remains constant at an applied voltage lower than 0.7 *V* and increases slowly at applied voltage higher than 0.7 *V*. The two *I–V* curves show a typical M–S Schottky feature and a marked nonlinearity, and the nonlinearity is more obvious for SL1. This kind of *I–V* response is very stable and repeatable, as demonstrated in Fig. 22b for the second time measurement. This result indicates that the superlattice

nanowires with a smaller bilayer thickness have a better electrical conductance and might thus have a better thermoelectric performance.

## CONCLUSIONS

In this manuscript, we have presented a short review on the fabrication and properties of 1D Bi-based nanostructures in our group. Although there are few results of thermoelectric performances in these nanostructures in the literature, it is still interesting to explore new routes to fabricate Bi-based nanostructures in the future, because many issues remain to be solved. Firstly, it is urgent to design the facile and effective measurement tools to obtain convincing thermoelectric data in an individual nanostructure; secondly, up to now, the fabrication technique for alloy nanotubes is very limited and finding new methods is still challenging; finally, superlattice nanostructures are the ultimate objectives for largely improving thermoelectric performance. We believe that 1D Bi-based nanostructures will have a brilliant future.

## ACKNOWLEDGMENTS

The authors acknowledge the support from the National Natural Science Foundation of China (No. 10704074, 10904145) and National Major Project of Fundamental Research for Nanomaterials and Nanostructures (No. 2005CB623603).

## REFERENCES

1. Z. B. Zhang, X. Z. Sun, M. S. Dresselhaus, J. Y. Ying. *Appl. Phys. Lett*. **73**, 1589 (1998).
2. L. D. Hicks, M. S. Dresselhaus. *Phys. Rev. B* **47**, 12727 (1993).
3. Y. M. Lin, O. Rabin, S. B. Cronin, J. Y. Ying. *Appl. Phys. Lett*. **81**, 2403 (2002).
4. M. S. Dresselhaus, G. Chen, M. Y. Tang, R. Yang, H. Lee, D. Wang, Z. Ren, P. Gogna. *Adv. Mater*. **19**, 1043 (2007).
5. D. S. Xu, X. S. Shi, G. L Guo, L. L. Gui, Y. Q. Tang. *J. Phys. Chem. B* **104**, 5061 (2000).
6. Q. Xu, L. Zhang, J. Zhu. *J. Phys. Chem. B* **107**, 8294 (2003).
7. W. Y. Li, L. N. Xu, J. Chen. *Adv. Funct. Mater*. **15**, 851 (2005).
8. Y. G. Guo, J. S. Hu, H. P. Liang, L. J. Wan, C. L. Bai. *Adv. Funct. Mater*. **15**, 196 (2005).
9. Y. G. Guo, L. J. Wan, C. L. Bai. *J. Phys. Chem. B* **107**, 5441 (2003).
10. T. Li, S. G. Yang, L. S. Huang, B. X. Gu, Y. W. Du. *Nanotechnology* **15**, 1479 (2005).
11. N. Zhao, L. Fu, L. Yang, T. Zhang, G. Wang, Y. Wu, T. v. Ree. *Pure Appl. Chem*. **80**, 2283 (2008).
12. N. Zhao, G. Wang, Y. Huang, B. Wang, B. Yao, Y. Wu. *Chem. Mater*. **20**, 2612 (2008).
13. H. Q. Wang, G. H. Li, L. C. Jia, L. Li, G. Z. Wang. *Chem. Commun*. 3786 (2009).
14. H. Q. Wang, G. H. Li, L. C. Jia, G. Z. Wang, L. Li. *Appl. Phys. Lett*. **93**, 153110-1 (2009).
15. H. Q. Wang, G. Z. Wang, L. C. Jia, C. J. Tang, G. H. Li. *J. Phys. Chem. C* **111**, 14307 (2007).
16. X. S. Fang, C. H. Ye, L. D. Zhang, J. X. Zhang, J. W. Zhao, P. Yan. *Small* **1**, 422 (2005).
17. T. Y. Zhai, X. S. Fang, Y. Bando, Q. Liao, X. J. Xu, H. B. Zeng, Y. Ma, J. N. Yao, D. Golberg. *ACS Nano* **3**, 949 (2009).
18. C. G. Jin, G. W. Jiang, W. F. Liu, W. L. Cai, L. Z. Yao, Z. Yao, X. G. Li. *J. Mater. Chem.* **13**, 1743 (2003).
19. G. Bhimarasetti, M. K. Sunkara. *J. Phys. Chem. B* **109**, 16219 (2005).
20. J. Heremans, C. M. Thrush, Z. Zhang, X. Sun, M. S. Dresselhaus, J. Y. Ying, D. T. Morelli. *Phys. Rev. B* **58**, R 10091 (1998).
21. L. Li, Y. Zhang, G. H. Li, L. D. Zhang. *Chem. Phys. Lett*. **378**, 244 (2003).
22. L. Li, Y. Zhang, G. H. Li, X. W. Wang, L. D. Zhang. *Mater. Lett*. **59**, 1223 (2005).

 

23. L. Li, Y. Zhang, Y. W. Yang, X. H. Huang, G. H. Li, L. D. Zhang. *Appl. Phys. Lett*. **87**, 031912 (2005).
24. Y. D. Li, J. W. Wang, Z. X. Deng, Y. Y. Wu, X. M. Sun, D. P. Yu, P. D. Yang. *J. Am. Chem. Soc*. **123**, 9904 (2001).
25. X. Y. Liu, J. H. Zeng, S. Y. Zhang, R. B. Zheng, X. M. Liu, Y. T. Qian. *Chem. Phys. Lett*. **374**, 348 (2003).
26. L. Li, Y. W. Yang, X. H. Huang, G. H. Li, R. Ang, L. D. Zhang. *Appl. Phys. Lett*. **88**, 103119 (2006).
27. J. P. Michenaud, J. P. Issi. *J. Phys. C* **5**, 3061 (1972).
28. Y. Zhang, L. Li, G. H. Li. *Nanotechnology* **16**, 2096 (2005).
29. Y. Zhang, L. Li, G. H. Li, L. D. Zhang. *Phys. Rev. B* **73**, 113403 (2006).
30. L. Li, G. H. Li, Y. Zhang, Y. W. Yang, L. D. Zhang. *J. Phys. Chem. B* **108**, 19380 (2004).
31. L. Li, Y. W. Yang, X. H. Huang, G. H. Li, L. D. Zhang. *Nanotechnology* **17**, 1706 (2006).
32. R. Venkatasubramanian, E. Siivola, T. Colpitts, B. O'Quinn. *Nature* **413**, 597 (2001).
33. M. S. Sander, R. Gronsky, T. Sands, A. M. Stacy. *Chem. Mater.* **15**, 335 (2003).
34. A. L. Prieto, M. S. Sander, M. Martín-González, R. Gronsky, T. Sands, A. M. Stacy. *J. Am. Chem. Soc*. **123**, 7160 (2001).
35. L. Li, Y. Zhang, G. H. Li, W. H. Song, L. D. Zhang. *Appl. Phys. A* **80**, 1053 (2005).
36. X. C. Dou, G. H. Li, X. H. Huang, L. Li. *J. Phys. Chem. C* **112**, 8167 (2008).
37. X. C. Dou, G. H. Li, H. C. Lei, X. H. Huang, L. Li, I. W. Boyd. *J. Electrochem. Soc*. **156**, K149 (2009).
38. X. C. Dou, G. H. Li, H. C. Lei. *Nano Lett.* **8**, 1286 (2008).

 